Position and Orientation from Asynchronous Lidar in GNSS Denied Environments

Craig Glennie[1], Francisco Haces-Garcia[1]

[1] University of Houston, Department of Civil & Environmental Engineering
5000 Gulf Freeway, Houston, TX USA- (clglennie, fhacesgarcia)@uh.edu

Keywords: GNSS Jamming, Spoofing, Asynchronous Lidar

Abstract

This study investigates the use of a distributed asynchronous lidar system for augmented position and orientation determination in Global Navigation Satellite Systems (GNSS) denied environments. An asynchronous lidar design is one in which the laser transmitter and detectors/receivers are disconnected and carried on separate platforms. This unique geometry offers observational redundancy that can be used to estimate the trajectory of the receiver platforms. The paper presents the results of simulation experiments, first examining single epoch solutions and then considers estimates of position and orientation along simulated flight trajectories. The results show that as long as the laser transmitter is operated above the GNSS denied environment, the system is able to simultaneously estimate position and orientation for multiple receiver drones, even for extended periods of GNSS outages. The accuracy of position and orientation estimation is dependent on the exact flight path and the number of lidar receivers in the solution, but with favorable geometry the accuracy of position estimation can approach that provided by a high precision GNSS solution.

1. Introduction

The use of Global Navigation Satellite Systems (GNSS) has become ubiquitous in modern life. The applications of GNSS have expanded well beyond the original requirements for global positioning and navigation. Now, GNSS systems are also used for a variety applications which require precise timing and synchronization such as in mobile networks, autonomous vehicles and real-time data transmission. While the use of GNSS is ubiquitous, it is also vulnerable to spoofing and jamming due to the physical and structural characteristics of the one-way time of arrival signals. The systems have extremely low power levels (around –160 dBW) at the Earth’s surface, making them easily overpowered by local near-surface based transmitters (Humphreys et al., 2008). Most civilian GNSS signals are not encrypted; they have open-source documentation that allows easy generation of counterfeit signals that closely mimic legitimate ones (Psiaki and Humphreys, 2016). Furthermore, GNSS signals utilize known frequency bands and require line-of-sight transmission, rendering them susceptible to interference (Wesson et al., 2012). Collectively, these limitations render GNSS systems prone to spoofing and jamming (Dovis, 2015), posing serious risks to position, navigation, timing (PNT) applications dependent on their accuracy and integrity.

Detection and mitigation of both jamming and spoofing is an open area of research. A majority of active research can be divided into three categories: (1) sensor fusion, (2) enhancements to receiver autonomous integrity monitoring (RAIM) using signals of opportunity, and (3) machine learning approaches. Sensor fusion leverages the addition of other navigation or dead-reckoning observations to GNSS positioning, such as the use of inertial measurement units (IMUs), or low-cost speedometer and magnetometer sensors, see for example (Dasgupta et al., 2022, Guizzaro et al., 2022). These approaches primarily rely upon examining positioning differences between the GNSS receiver and the predicted motion using the IMU and/or dead reckoning sensors. RAIM techniques for GNSS are well established in the literature, and rely upon an examination of relative consistency among individual satellite signals. Because this technique requires solution redundancy, and could be exploited by spoofing on all satellite channels, recent investigations have looked at using other available signals of opportunity such as Wi-Fi or cellular signals (Liu and Papadimitratos, 2024), that can be used to provide independent estimates of position and velocity (Jia and Kassas, 2022). Recently, the most active area of research has been the application of machine learning and artificial intelligence to GNSS spoofing and jamming. A variety of techniques have been investigated. For example, (Morales Ferre et al., 2019) compare the use of support vector machines and convolutional neural networks for GNSS jammer classification, while (Gallardo et al., 2024) use a satellite signal analysis technique based on fingerprinting and machine learning with a fingerprinting metric based on the satellite instrumental delay. The number of machine learning approaches to spoofing and jamming detection have exploded in the literature and are too vast to enumerate here. The reader is referred to a relatively recent overview of machine learning techniques in the review paper by (Radoš et al., 2024).

With the development of GNSS software defined radios (Akos et al., 2022), the generation and broadcast of realistic spoofing signals is making it harder to separate real and fake signals, even using machine learning approaches. Therefore, methods that utilize external independent sensors may be a more promising avenue of future research. The use of inertial sensors, speedometers and magnetic compasses continue to be explored, as mentioned earlier, however these sensors all suffer from sensor drift which degrades their independent positioning accuracy, making them problematic for long-term positioning in GNSS denied environments. Along these lines, recent research has examined using photogrammetry (Meng et al., 2025) as an independent positioning solution for GNSS anomaly detection. While the results are promising, photogrammetric processing can be time and computer resource intensive, and, because it is a passive approach, it is reliant upon an imaging scene with enough texture for feature mapping and an external illumina-

This contribution has been peer-reviewed. The double-blind peer-review was conducted on the basis of the full paper.
https://doi.org/10.5194/isprs-annals-XI-1-2026-151-2026 | © Author(s) 2026. CC BY 4.0 License.

tion source (i.e. sunlight). Therefore, an active illumination technique with potentially less computational resources would be advantageous. Recent simulation and laboratory demonstrations of an asynchronous lidar system (Glennie et al., 2025) would seem to offer a promising alternative as its unique design provides observational redundancy that could be leveraged for bridging areas with GNSS jamming and perform as an independent positioning source for detection of spoofing. The asynchronous lidar technique decouples the laser transmitter and detectors, allowing them to fly on separate platforms, while also enabling multiple detectors to simultaneously observe the same laser impingement points; this cooperative sensing greatly increases the observational redundancy of the system. Therefore, we will examine the use of asynchronous lidar systems for providing precise positioning in GNSS-denied areas through a series of simulations. The remainder of the paper is organized as follows: Section 2 gives a brief description of GNSS jamming and spoofing along with a brief introduction to the concept of asynchronous lidar, Section 3 shows the modification of the conventional asynchronous lidar problem to enable geolocation, Section 4 describes the simulations that were performed, Section 5 provides a discussion of the simulation results and finally Section 6 wraps up the analysis with conclusions and possible directions for future work.

2. Background

2.1 GNSS Jamming and Spoofing

GNSS jamming is generally methods that attempt to prevent a GNSS receiver from obtaining a usable GNSS signal; they can be broadly labeled as denial or interference techniques. Jamming for GNSS generally entails the transmission of a high-power electromagnetic signal in the L frequency bands, with the intention of overloading the GNSS receiver so that it loses lock on actual satellite signals. Jamming can be quite problematic because jamming devices are relatively simple to design, build and operate. GNSS jammers are normally operated on the ground, near users. Because of radiative power loss, the effectiveness of jamming sources decreases as the distance from the jammer is increased - this means that higher flying drones (for example) are less susceptible to ground based jamming than lower flying drones, as illustrated in the right hand panel of Figure 1.

Spoofing on the other hand is a more complicated deception technique in which the spoofer presents counterfeit GNSS signals that appear genuine to the receiver (see left hand panel of Figure 1). The result is that the receiver calculates incorrect PNT parameters. The spoofer sends similar signals to those from GNSS satellites by replicating the carrier frequency, PRN code and information content of open source GNSS signals; these are normally transmitted at a slightly higher power to be selected over the actual satellite signals. The deceptive signals are normally either created using GNSS simulators or from a software defined radio that collects the authentic GNSS signals, modifies them (simplest method is a time delay) and then retransmits them. The increased level of sophistication for spoofing attacks make them much harder to detect than jamming or interference, however the cost is higher complexity for the spoofing system. A detailed overview of spoofing and jamming, along with strategies for detecting attacks can be found in the recent review paper by (Radoš et al., 2024), or in (Psiaki and Humphreys, 2016).

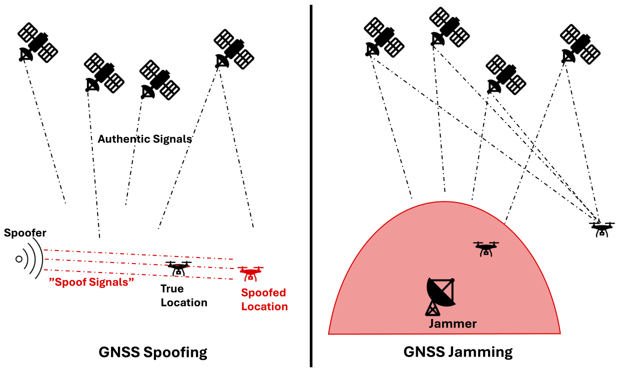

Figure 1. GNSS Spoofing (Left) and Jamming (Right)

2.2 Asynchronous Lidar

For the purposes of this paper, an asynchronous lidar system is defined as one where the laser transmitter and detector(s) are carried on separate airborne platforms, with no physical interconnections. Multiple receivers may therefore simultaneously detect the same laser impingement points. A GNSS/IMU navigation system is required for each of the transmitter and detector platforms to provide position, orientation and precise timing. A detailed derivation of the asynchronous lidar system equations is given in (Glennie et al., 2025), and is summarized here. Given a laser impingement point on the ground, the coordinates of that point can be written in terms of the lidar forward equation from the laser transmitter as:

$$\vec{\boldsymbol{r}}_g = \vec{\boldsymbol{r}}_t + \boldsymbol{R}^l_{b_t}(\boldsymbol{R}^b_{s_t} d_t \vec{\boldsymbol{u}}_t + \vec{\boldsymbol{l}}_t) \tag{1}$$

where $\vec{\boldsymbol{r}}_g = [X_g, Y_g, Z_g]^T$ are the coordinates of the ground point, $\vec{\boldsymbol{r}}_t = [X_t, Y_t, Z_t]^T$ are the coordinates of the transmitter, determined by the GNSS system, $\boldsymbol{R}^l_{b_t}$ is the IMU derived rotation matrix from the body frame of the transmitter to the local level coordinate frame, $\boldsymbol{R}^b_{s_t}$ is the misalignment of the scanner frame (boresight), d_t is the transmitter-to-ground distance, $\vec{\boldsymbol{u}}_t$ is the unit vector from the transmitter to the ground point in the laser frame, and $\vec{\boldsymbol{l}}_t$ is the lever arm offset. Similarly, we can define the corresponding equation for the laser light incident on the detector as:

$$\vec{\boldsymbol{r}}_g = \vec{\boldsymbol{r}}_r + \boldsymbol{R}^l_{b_r}(\boldsymbol{R}^b_{s_r} d_r \vec{\boldsymbol{u}}_r + \vec{\boldsymbol{l}}_r) \tag{2}$$

where $\vec{\boldsymbol{r}}_r = [X_r, Y_r, Z_r]^T$ are the coordinates of the receiver, determined by the GNSS system, $\boldsymbol{R}^l_{b_r}$ is the IMU derived rotation matrix from the body frame of the receiver to the local level coordinate frame, $\boldsymbol{R}^b_{s_r}$ is the misalignment of the detector frame (boresight), d_r is the receiver-to-ground distance, $\vec{\boldsymbol{u}}_r$ is the unit vector from the receiver to the ground point in the laser frame, and $\vec{\boldsymbol{l}}_r$ is the receiver lever arm offset. The geometry of the transmitter and receiver, along with the major terms in the above equations are graphically depicted in Figure 2. Equations 1 and 2 are both expressed in terms of the ground coordinates and therefore the right hand sides of each equation can be set equal to one another, obtaining:

$$\vec{\boldsymbol{r}}_t + \boldsymbol{R}^l_{b_t}(\boldsymbol{R}^b_{s_t} d_t \vec{\boldsymbol{u}}_t + \vec{\boldsymbol{l}}_t) = \vec{\boldsymbol{r}}_r + \boldsymbol{R}^l_{b_r}(\boldsymbol{R}^b_{s_r} d_r \vec{\boldsymbol{u}}_r + \vec{\boldsymbol{l}}_r) \tag{3}$$

The lever arms and boresight parameters on both sides of Equation 3 are constants and can be independently determined using standard lidar boresight calibration methods (e.g. (Skaloud and Lichti, 2006)) and/or photogrammetric bundle block adjustment techniques (Lichti et al., 1997). Then, assuming that both the transmitter and receiver platforms have positioning and orientation systems (i.e. GNSS and IMU) onboard, as is standard for airborne lidar, Equation 3 provides at set of three equations with only two unknowns; namely the distances d_r and d_t. Thus, this formulation of an asynchronous lidar system provides observational redundancy that is missing from conventional single platform airborne laser scanners (Glennie, 2007). This redundancy can then be exploited, especially in cases with multiple simultaneous receivers or multiple coincident laser impingement points. In general, each additional receiver provides and additional two degrees of freedom, while an additional coincident impingement point increases redundancy by one. Overall, the number of observations, number of unknowns and observational redundancy can be computed (assuming one transmitter) as a function of the number of coincident laser points and receivers as:

$$n = 3R_x P_g \tag{4}$$

$$u = 2(R_x + P_g) \tag{5}$$

where n is the number of observations, u is the number of unknowns, R_x is the number of receiver platforms and P_g is the number of coincident laser points. Redundany (r) is then simply calculated as:

$$r = n - u \tag{6}$$

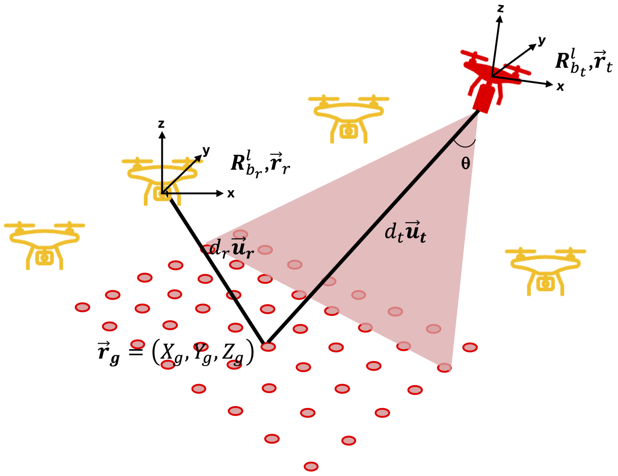

Figure 2. Configuration of an Asynchronous Lidar System. Red drone indicates transmitter, and yellow drones are receivers.

3. Methods

The observational redundancy of an asynchronous lidar system motivates an investigation of what additional parameters can be solved for by leveraging the system. In this instance, we contemplate that occasional jamming and/or spoofing of the GNSS signal might be present within the theater of operation of the asynchronous lidar system and we would like to investigate if errors due to jamming or spoofing can be (a) detected and (b) mitigated using the additional system observational redundancy.

To examine the added capabilities for jamming detection from a redundant asynchronous lidar system, the first stage of this work focuses on the extension of the conventional asynchronous lidar problem to determine the location of receivers in stationary scenarios. If stationary receivers can be robustly geolocated using solely asynchronous lidar, the technique can then be used for GNSS jamming detection. The second stage of this manuscript deploys the concept in-flight for a UAS to demonstrate how asynchronous lidar can also be used determine the kinematic location of receiver(s).

3.1 Geolocation using Asynchronous Lidar

The optimal configuration of an asynchronous lidar system presented in (Glennie et al., 2025), has the transmitter flying at a higher elevation AGL (above ground level) than the receiver drones. This configuration would also be convenient for spoofing or jamming detection and avoidance, if we consider the transmitter flying at an AGL out of range of ground-based spoofing or jamming sources; thus the position and orientation of the transmitter can be obtained with high reliability. In this case, equation (3) can be rearranged to not only solve for the point on the ground, but also for the position and orientation of the receiver platforms. We can rearrange the equation as:

$$\vec{\boldsymbol{F}} = \vec{\boldsymbol{r}}_t = \vec{\boldsymbol{r}}_r - \boldsymbol{R}^l_{b_t}(d_t\vec{\boldsymbol{u}}_t) + \boldsymbol{R}^l_{b_r}(d_r\vec{\boldsymbol{u}}_r) \tag{7}$$

There are 8 unknowns in this equation, the three components of $\vec{\boldsymbol{r}}_r$, the Euler angles ω,ϕ and κ from $\boldsymbol{R}^l_{b_r}$, and the two distances d_r and d_t. This equation is a parametric model, i.e. $l = f(x)$ and can be solved using parametric least squares, where the design matrix $\boldsymbol{A}$ and the observation equation partial derivatives are given in Appendix A. For each additional receiver with unknown position and orientation, an additional 7 unknowns (6 exterior orientation parameters and a range to the target point) are added as columns to the A-matrix.

3.2 Solution to Functional Equation

Parametric least squares was implemented to solve Equation (7) and demonstrate the jamming detection and geolocation capabilities of an asynchronous lidar system. Specifically, solutions from this system of equations were obtained using a weighted non-linear least squares solution solved using Scipy’s Trust Region Reflective algorithm (Coleman and Li, 1996). The Jacobian function (shown in Appendix A, Equation 8) was built using symbolically-generated partial derivatives, which were evaluated analytically at each iteration of the function call to avoid unnecessary linearization of the least squares solution.

3.3 Single-Epoch Simulation

Without loss of generality, a single-transmitter multi-beam asynchronous lidar system was selected for simulation, and validated with data collected from a laboratory demonstration. A variety of initialization values and weak Gaussian priors were tested to examine the robustness of the solution convergence. The test scenarios are detailed in Table 1, and were selected to represent several realistic operational scenarios for asynchronous lidar geolocation systems, with Gaussian priors used to constrain certain solutions. Experiment 1 represents a system in which a single receiver is undergoing jamming. Experiment 2 extends experiment 1 with the assumption that an onboard IMU can generally provide only time-degraded IMU mechanized orientation. Similarly, Experiment 3 represents a system in which receiver orientations are approximately known, but all receivers have lost GNSS signal. Within the scale of the laboratory demonstration herein, these values represent conservative estimates. Some potential real-world values for these uncertainties are discussed in Section 5.1.

Experiment #	Gaussian Priors	# of Known R_x Positions	# of Unknown R_x
1	None	1-8	1
2	Initial R_x, Orientation error $< 5°$	1-8	1
3	Initial R_x, Orientation error $< 5°$	0	1-8

Table 1. Configurations for asynchronous lidar single-epoch tests with a single transmitter and 8 receivers (R_x).

3.3.1 Laboratory Demonstration The laboratory demonstration used herein was similar to that described in (Glennie et al., 2025); for completeness, it is detailed in this section but the reader is referred to the original publication for full implementation details. The data obtained is valuable to examine the accuracy of receiver geolocation with asynchronous lidar in a real-world deployment. It’s use also enables direct comparison to the accuracy of the conventional asynchronous lidar problem. A transmitter with 101 beams was implemented with eight receivers, with varied observational geometries. The external and internal orientation parameters for each receiver were independently obtained using a self-calibrating photogrammetric bundle adjustment (Lichti et al., 1997).

3.3.2 Geolocation Accuracy Assessment An asynchronous lidar system can be configured to have an arbitrary amount of receivers. Several configurations were tested in this work to examine their impact on geolocation accuracy. For each receiver, all possible configurations with the remaining receivers in the laboratory setup were obtained, with the total number of receivers per configuration varying from one to eight. Then, the experiments detailed in Table 1 were performed, estimating the location of one (or several) receivers. These position estimates were compared to the measured positions in the laboratory setting to independently assess geolocation accuracy.

3.4 Mobile Geolocation

GNSS jamming results in IMU only positioning for UAS navigation, resulting in position and orientation errors which grow exponentially with time. Given the robustness of an asynchronous lidar system, and it’s ability to operate independently from other flight sensors, using it as a supplement for in-flight geolocation and orientation warrants study. A series of experiments were performed to geolocate a simulated flying receiver within the described laboratory setup. Three different flight patterns were tested, with the receiver oriented towards the center of the laser pattern in flight. Given the sensitivity of asynchronous lidar to various network geometries, the variability of geolocation accuracy for a straight line simulation was also examined across several network geometries. The amount of receivers with known positions was also varied. The flight patterns used for examination are shown in Figure 3, which shows their relative location within the test geometry of the laboratory demonstrations.

Mobile geolocation experiments were performed by selecting one of the three flight paths depicted in Figure 3. IMU drift for the flying receiver was estimated as a compounding error of 1° per minute of GNSS denied flight. Flights had a total jamming duration of 2 minutes, during which position was estimated every second using dead reckoning.; IMU errors introduced compounding position and orientation errors to these dead reckoning estimates. Thus, for each iteration, the dead reckoning estimate was used as the initial value for an asynchronous lidar position estimate. The external orientation parameters for the simulated receiver were then obtained using the updated position. Both the updated position and orientation were compared to the known values from the simulated flight path.

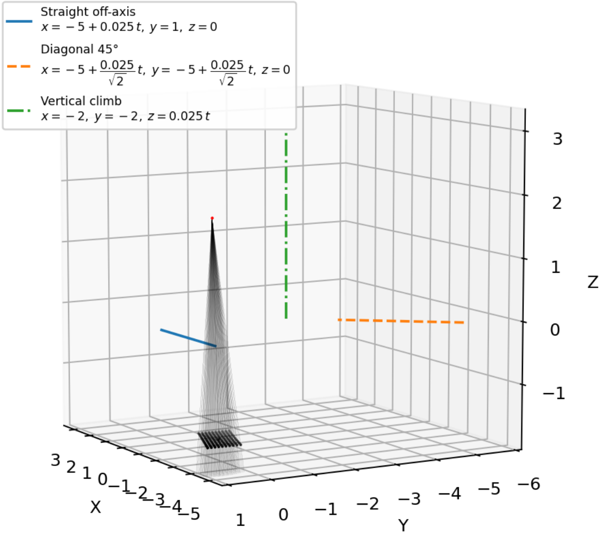

Figure 3. Geometry of simulations used for the testing of Asynchronous Lidar Geolocation. Dashed lines indicate simulated trajectories. Red dot is transmitter location, with 101 laser beams projected on ground surface.

4. Results

The results section is structured as follows: first, the results obtained from the various single-epoch geolocation experiments are presented. Then, the simulations for mobile geolocation of an asynchronous lidar system are given.

4.1 Single-Epoch Geolocation

4.1.1 Single unknown receiver (Experiments 1 and 2) Figure 4 shows the 3D residuals for position estimates for each receiver for all possible network configurations without any prior information. It is noted that for a configuration with a total of n receivers, the total number of potential estimates can be calculated as $n * \binom{n_{total}}{n}$, where n_{total} refers to the total number of receivers in the configuration. As shown in the figure, the median residual varies slightly by the number of known receivers in the simulation, with a point of diminishing returns being reached around three or four receivers. This corroborates previous results in (Glennie et al., 2025) for estimating ground impingement points with an asynchronous lidar system. Notably, the residuals for geolocation are approximately an order of magnitude larger than those reported for ground coordinates in the previous study. Thus, this motivates the study of whether prior information about the asynchronous lidar configuration can be used to improve the overall accuracy of the solution.

Experiment 2 repeats the simulations shown in Figure 4, but now seeds initial estimates for receiver orientation within 5° for the least squares solution. The results are shown in Figure 5. The solution accuracy improves by about an order of magnitude when compared to Experiment 1, likely because the

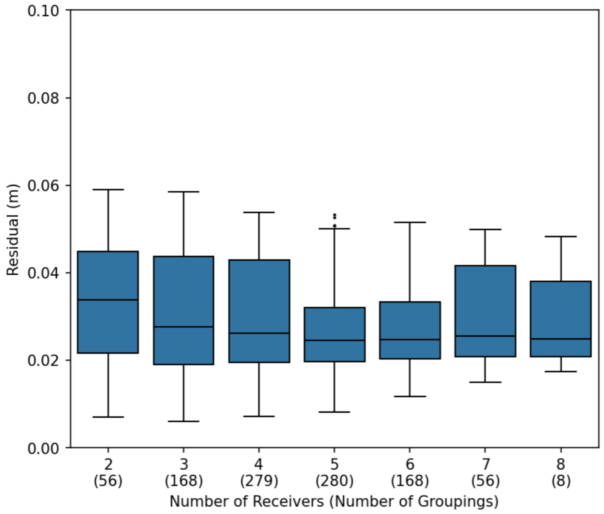

Figure 4. 3D Residuals for Single-Epoch Geolocation using Asynchronous Lidar with no prior information.

Jacobian matrix in the least squares solution is now better constrained. This makes geolocation accuracy comparable to that obtained for ground impingement points using asynchronous lidar in labratory demonstrations. The accuracy dependence on the amount of known receivers is not observed in this experiment - 3D residuals are fairly uniform across all tested numbers of receivers. Experiment 2 demonstrates the value of coarse initial estimates of orientation to seed the least squares solution.

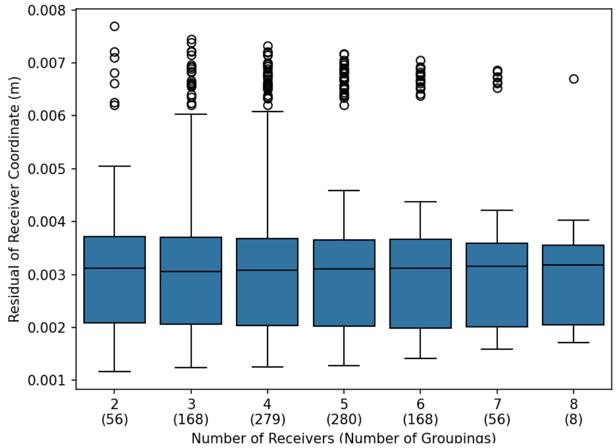

Figure 5. 3D Residuals for Single-Epoch Geolocation using Asynchronous Lidar with Coarse Initial Estimates for Receiver Orientation (within 5°).

4.1.2 No known receivers (Experiment 3) Given the robustness of the system of equations used for geolocation in asynchronous lidar, and the improved accuracy resulting from the inclusion of coarse orientation information (as shown in Experiment 2), it is worthwhile to examine whether any known receiver positions at all are required to estimate geolocation for all receivers. Thus, Experiment 3 performs similar simulations to the prior experiments, but instead of attempting to position a single receiver, it attempts to position all receivers simultaneously. There are $\binom{n_{total}}{n}$ groupings for this experiment, which included the same initial orientation seed estimates as Experiment 2 (5°). The results are shown in Figure 6. Surprisingly, for a majority of groupings ($n = 136/255$), we are able to obtain solutions comparable to those in Experiment 1 (location residuals under 5 cm). This demonstrates that in GNSS-denied scenarios, with coarse orientation information, the strong geometry of an asynchronous lidar solution, is enough to adequately condition the Jacobian matrix and geolocate a multitude of receivers. The robustness of the solution can, of course, be improved by adding additional transmitters or constraints to the search space.

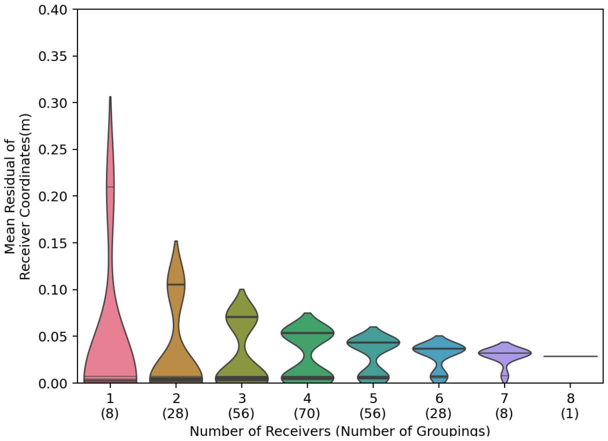

Figure 6. 3D Residuals for Single-Epoch Geolocation using Asynchronous Lidar with no known receiver positions. Initial receiver orientation assumed to be within 5°. Horizontal lines denote individual observations.

4.2 Mobile Geolocation

Given the success of single-epoch geolocation for unknown receivers, the study of using an asynchronous lidar system to position a mobile receiver during flight was warranted. Simulations were performed both without incorporating Gaussian priors in the least squares solution, and using dead reckoning estimates at each epoch for initial least squares estimates. A comparison of the positioning accuracy for each flight path is shown in Figure 7. As depicted, mobile geolocation achieves similar levels to that achieved for single-epoch geolocation (Experiment 1). Flight geometry appears to play a key role in geolocation accuracy, with horizontal flights (along XY plane) having higher accuracy in our testing than vertical flight.

4.2.1 Sensor Number Dependence Figure 8 shows the accuracy achieved across flight paths with respect to the amount of known receivers in the simulation. As shown, there is a significant accuracy dependence on the amount of known sensors. While this does not immediately correlate with the results observed in the single-epoch geolocation experiments, it is noted that these simulations rely on multiple sequential position estimates from asynchronous lidar. Thus, while the benefits of additional sensors may not be as apparent in single-shot experiments, their accumulated presence in mobile simulations drastically improved performance.

5. Discussion

The simulations performed herein demonstrate that receiver geolocation can be achieved with an extension of the conventional asynchronous lidar solution. Across both single-epoch

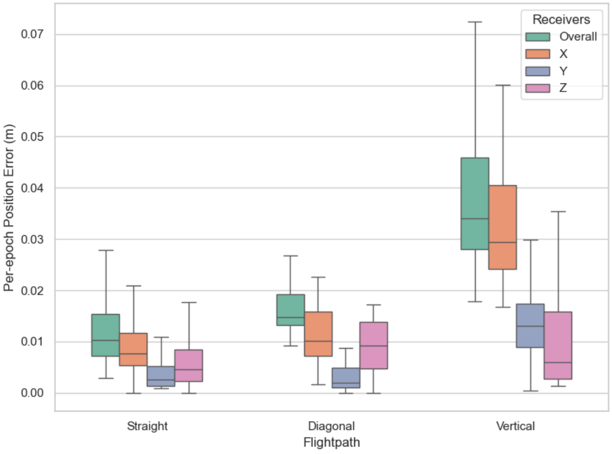

Figure 7. Residuals of asynchronous lidar geolocation for each flight path.

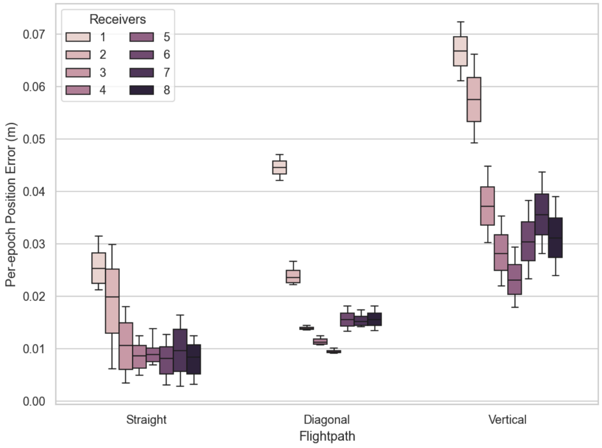

Figure 8. 3D position residuals for asynchronous lidar geolocation simulations in continuous flight across various flight paths and receiver configurations.

and mobile settings, geolocation accuracies reached levels comparable with bundle adjustment accuracies. The stationary geolocation of a single receiver with initial coarse orientation estimates (Experiment 2) achieves similar accuracy levels to those observed previously in (Glennie et al., 2025). While the benefits of multiple independent receivers were not immediately apparent in single-epoch experiments (Experiments 1 and 2), the mobile simulations across different flightpaths demonstrated that they can significantly improve geolocation accuracy.

5.1 Insights from Experimentation

The experiments showed significant geolocation accuracy improvements with coarse intital estimates of receiver orientation (within 5°). In real-world scenarios, this can generally be obtained from the last known IMU estimate at GNSS jamming onset. As suggested by our mobile experiment, continuous updates to receiver orientation can be obtained from the asynchronous lidar solution, which would mitigate the accretion of IMU drift in GNSS-denied environments. While these values are not strictly required to perform geolocation (as demonstrated by Experiment 1), they are both practical to obtain in real-world settings and useful to improve the overall accuracy of the asynchronous lidar solution.

The simulations performed herein relied on a single transmitter to perform geolocation. While the motivation behind this choice was to demonstrate that geolocation was viable with a minimal setup, there are relevant benefits to the use of multiple transmitters in GNSS-denied environments. Beyond potential accuracy improvements and additional robustness in the least squares solution, the use of multiple transmitters also enlarges the operational footprint of the geolocation solution. Specifically, multiple transmitters may be used to mitigate both optical occlusions and poor observation geometries in mobile scenarios. While this work demonstrates that continuous geolocation using asynchronous lidar is possible, a practical implementation of such a system may use additional transmitters for operational robustness.

5.2 GNSS Spoofing Detection

The detection of GNSS spoofing has emerged as a key challenge for the geolocation of mobile receivers. The increasing levels of sophistication of such attacks motivate the study of potential detection and/or mitigation techniques. The literature has explored signal quality monitoring, radio frequency fingerprinting, and artificial intelligence, among other techniques (Radoš et al., 2024). While these techniques are useful, they may remain susceptible to future developments. Within this context, the demonstrated effectiveness of asynchronous lidar geolocation in GNSS jamming scenarios indicates the potential for it to serve as a independent check for GNSS spoofing. The results shown in Experiment 3 demonstrate that there exists great potential for the solution of asynchronous lidar systems without any known receiver positions. These results also suggest that asynchronous lidar geolocation can be a useful independent measurement to detect GNSS spoofing.

6. Conclusions and Future Work

GNSS jamming and spoofing are key challenges in the accurate and reliable determination of PNT. Recent work in (Glennie et al., 2025) developed a robust asynchronous lidar technique for the detection of ground points from decoupled transmitters and receivers. This work extends that technique to solve for receiver positions in GNNS-denied environments. Through several simulations, we demonstrate that asynchronous lidar geolocation is an efficient avenue to mitigate GNSS jamming in both single-epoch and mobile settings. Several areas of future research are being actively pursued. Field deployments of an asynchronous lidar system mounted on several UAS platforms are undergoing testing and development. Moreover, multiple transmitter systems are being investigated as a potential solution for some of the possible issues with the field deployment of asynchronous lidar geolocation. Finally, the operational demonstration of spoofing detection using asynchronous lidar geolocation is also under investigation.

References

Akos, D., Arribas, J., Bhuiyan, M. Z. H., Closas, P., Dovis, F., Fernandez-Hernandez, I., Fernández-Prades, C., Gunawardena, S., Humphreys, T., Kassas, Z. M. et al., 2022. Gnss software defined radio: history, current developments, and standardization efforts. *Proceedings of the 35th International Technical Meeting of the Satellite Division of The Institute of Navigation (ION GNSS+ 2022)*, 3180–3209.

Coleman, T. F., Li, Y., 1996. An interior trust region approach for nonlinear minimization subject to bounds. *SIAM Journal on optimization*, 6(2), 418–445.

Dasgupta, S., Rahman, M., Islam, M., Chowdhury, M., 2022. A Sensor Fusion-Based GNSS Spoofing Attack Detection Framework for Autonomous Vehicles. *IEEE Transactions on Intelligent Transportation Systems*, 23(12), 23559-23572.

Dovis, F. (ed.), 2015. *GNSS Interference Threats and Countermeasures*. Artech House, Norwood, MA.

Gallardo, F., Pérez-Yuste, A., Konovaltsev, A., 2024. Satellite Fingerprinting Methods for GNSS Spoofing Detection. *Sensors*, 24(23). https://www.mdpi.com/1424-8220/24/23/7698.

Glennie, C. L., 2007. Rigorous 3D error analysis of kinematic scanning LIDAR systems. *Journal of Applied Geodesy*, 1(3), 147–157.

Glennie, C. L., Bui, L. K., Haces-Garcia, F., Lichti, D. D., 2025. Asynchronous Lidar: Proof-of-concept simulation and demonstration tests. *ISPRS Open Journal of Photogrammetry and Remote Sensing*, 17, 100096.

Guizzaro, C., Formaggio, F., Tomasin, S., 2022. Gnss spoofing attack detection by imu measurements through a neural network. *2022 10th Workshop on Satellite Navigation Technology (NAVITEC)*, 1–6.

Humphreys, T. E., Ledvina, B. M., Psiaki, M. L., O’Hanlon, B. W., Kintner, P. M. et al., 2008. Assessing the spoofing threat: Development of a portable gps civilian spoofer. *Proceedings of the 21st International technical meeting of the satellite division of the institute of navigation (ION GNSS 2008)*, 2314–2325.

Jia, M., Kassas, Z. M., 2022. Kalman Filter-Based Integrity Monitoring for GNSS and 5G Signals of Opportunity Integrated Navigation. *IFAC-PapersOnLine*, 55(24), 273-278. 10th IFAC Symposium on Advances in Automotive Control AAC 2022.

Lichti, D., Chapman, M. et al., 1997. Constrained FEM self-calibration. *Photogrammetric engineering and remote sensing*, 63(9), 1111–1119.

Liu, W., Papadimitratos, P., 2024. Extending raim with a gaussian mixture of opportunistic information. *Proceedings of the 2024 International Technical Meeting of The Institute of Navigation*, 454–466.

Meng, C., Yang, H., Jiang, C., Hu, Q., Li, D., 2025. Improving UAV Remote Sensing Photogrammetry Accuracy Under Navigation Interference Using Anomaly Detection and Data Fusion. *Remote Sensing*, 17(13). https://www.mdpi.com/2072-4292/17/13/2176.

Morales Ferre, R., de la Fuente, A., Lohan, E. S., 2019. Jammer Classification in GNSS Bands Via Machine Learning Algorithms. *Sensors*, 19(22). https://www.mdpi.com/1424-8220/19/22/4841.

Psiaki, M. L., Humphreys, T. E., 2016. GNSS Spoofing and Detection. *Proceedings of the IEEE*, 104(6), 1258-1270.

Radoš, K., Brkić, M., Begušić, D., 2024. Recent Advances on Jamming and Spoofing Detection in GNSS. *Sensors*, 24(13). https://www.mdpi.com/1424-8220/24/13/4210.

Skaloud, J., Lichti, D., 2006. Rigorous approach to bore-sight self-calibration in airborne laser scanning. *ISPRS Journal of Photogrammetry and Remote Sensing*, 61(1), 47-59.

Wesson, K., Shepard, D., Humphreys, T., 2012. Straight talk on anti-spoofing. *Gps World*, 23(1), 32–39.

Appendix A

$$\boldsymbol{A} = \begin{bmatrix} \frac{\partial X_{t,R_1}}{\partial X_r} & \frac{\partial X_{t,R_1}}{\partial Y_r} & \frac{\partial X_{t,R_1}}{\partial Z_r} & \frac{\partial X_{t,R_1}}{\partial \omega_r} & \frac{\partial X_{t,R_1}}{\partial \phi_r} & \frac{\partial X_{t,R_1}}{\partial \kappa_r} & \frac{\partial X_{t,R_1}}{\partial d_t} & \frac{\partial X_{t,R_1}}{\partial d_r} \\ \frac{\partial Y_{t,R_1}}{\partial X_r} & \frac{\partial Y_{t,R_1}}{\partial Y_r} & \frac{\partial Y_{t,R_1}}{\partial Z_r} & \frac{\partial Y_{t,R_1}}{\partial \omega_r} & \frac{\partial Y_{t,R_1}}{\partial \phi_r} & \frac{\partial Y_{t,R_1}}{\partial \kappa_r} & \frac{\partial Y_{t,R_1}}{\partial d_t} & \frac{\partial Y_{t,R_1}}{\partial d_r} \\ \frac{\partial Z_{t,R_1}}{\partial X_r} & \frac{\partial Z_{t,R_1}}{\partial Y_r} & \frac{\partial Z_{t,R_1}}{\partial Z_r} & \frac{\partial Z_{t,R_1}}{\partial \omega_r} & \frac{\partial Z_{t,R_1}}{\partial \phi_r} & \frac{\partial Z_{t,R_1}}{\partial \kappa_r} & \frac{\partial Z_{t,R_1}}{\partial d_t} & \frac{\partial Z_{t,R_1}}{\partial d_r} \\ \vdots & \vdots & \vdots & \vdots & \vdots & \vdots & \vdots & \vdots \\ \frac{\partial X_{t,R_N}}{\partial X_r} & \frac{\partial X_{t,R_N}}{\partial Y_r} & \frac{\partial X_{t,R_N}}{\partial Z_r} & \frac{\partial X_{t,R_N}}{\partial \omega_r} & \frac{\partial X_{t,R_N}}{\partial \phi_r} & \frac{\partial X_{t,R_N}}{\partial \kappa_r} & \frac{\partial X_{t,R_N}}{\partial d_t} & \frac{\partial X_{t,R_N}}{\partial d_r} \\ \frac{\partial Y_{t,R_N}}{\partial X_r} & \frac{\partial Y_{t,R_N}}{\partial Y_r} & \frac{\partial Y_{t,R_N}}{\partial Z_r} & \frac{\partial Y_{t,R_N}}{\partial \omega_r} & \frac{\partial Y_{t,R_N}}{\partial \phi_r} & \frac{\partial Y_{t,R_N}}{\partial \kappa_r} & \frac{\partial Y_{t,R_N}}{\partial d_t} & \frac{\partial Y_{t,R_N}}{\partial d_r} \\ \frac{\partial Z_{t,R_N}}{\partial X_r} & \frac{\partial Z_{t,R_N}}{\partial Y_r} & \frac{\partial Z_{t,R_N}}{\partial Z_r} & \frac{\partial Z_{t,R_N}}{\partial \omega_r} & \frac{\partial Z_{t,R_N}}{\partial \phi_r} & \frac{\partial Z_{t,R_N}}{\partial \kappa_r} & \frac{\partial Z_{t,R_N}}{\partial d_t} & \frac{\partial Z_{t,R_N}}{\partial d_r} \end{bmatrix} \tag{8}$$

The partial derivatives are given as:

$$\frac{\partial F}{\partial \vec{r_r}} = \begin{bmatrix} \frac{\partial X_{t,R_n}}{\partial X_r} \\ \frac{\partial Y_{t,R_n}}{\partial Y_r} \\ \frac{\partial Z_{t,R_n}}{\partial Z_r} \end{bmatrix} = \begin{bmatrix} 1 \\ 1 \\ 1 \end{bmatrix} \tag{9}$$

$$\frac{\partial F}{\partial d_t} = \begin{bmatrix} \frac{\partial X_{t,R_n}}{\partial d_t} \\ \frac{\partial Y_{t,R_n}}{\partial d_t} \\ \frac{\partial Z_{t,R_n}}{\partial d_t} \end{bmatrix} = -\boldsymbol{R}^l_{b_t} \vec{\boldsymbol{u}}_t \tag{10}$$

$$\frac{\partial F}{\partial d_r} = \begin{bmatrix} \frac{\partial X_{t,R_n}}{\partial d_r} \\ \frac{\partial Y_{t,R_n}}{\partial d_r} \\ \frac{\partial Z_{t,R_n}}{\partial d_r} \end{bmatrix} = \boldsymbol{R}^l_{b_r} \vec{\boldsymbol{u}}_r \tag{11}$$

$$\frac{\partial F}{\partial \omega} = \begin{bmatrix} \frac{\partial X_{t,R_n}}{\partial \omega} \\ \frac{\partial Y_{t,R_n}}{\partial \omega} \\ \frac{\partial Z_{t,R_n}}{\partial \omega} \end{bmatrix} = \frac{\partial \boldsymbol{R}^l_{b_r}}{\partial \omega} d_r \vec{\boldsymbol{u}}_r \tag{12}$$

$$\frac{\partial F}{\partial \phi} = \begin{bmatrix} \frac{\partial X_{t,R_n}}{\partial \phi} \\ \frac{\partial Y_{t,R_n}}{\partial \phi} \\ \frac{\partial Z_{t,R_n}}{\partial \phi} \end{bmatrix} = \frac{\partial \boldsymbol{R}^l_{b_r}}{\partial \phi} d_r \vec{\boldsymbol{u}}_r \tag{13}$$

$$\frac{\partial F}{\partial \kappa} = \begin{bmatrix} \frac{\partial X_{t,R_n}}{\partial \kappa} \\ \frac{\partial Y_{t,R_n}}{\partial \kappa} \\ \frac{\partial Z_{t,R_n}}{\partial \kappa} \end{bmatrix} = \frac{\partial \boldsymbol{R}^l_{b_r}}{\partial \kappa} d_r \vec{\boldsymbol{u}}_r \tag{14}$$